

Automated Delineation of Calcified Vessels in Mammography by Tracking With Uncertainty and Graphical Linking Techniques

Jie-Zhi Cheng, Chung-Ming Chen, Elodia B. Cole, Etta D. Pisano, and Dinggang Shen*, *Senior Member, IEEE*

Abstract—As a potential biomarker for women’s cardiovascular and chronic kidney diseases, breast arterial calcification (BAC) in mammography has become an emerging research topic in recent years. To provide more objective measurement for vascular structures with calcium depositions in mammography, a new computerized method is introduced in this paper to delineate the calcified vessels. Specifically, we leverage two underlying cues, namely calcification and vesselness, into a multiple seeded tracking with uncertainty scheme. This new vessel-tracking scheme generates plenty of sampling paths to describe the complicated topology of the vascular structures with calcium depositions. A compiling and linking process is further carried out to organize the sampling paths together to be the vessel segments that likely belong to the same vessel tract. The proposed method has been evaluated on 63 mammograms, by comparison with manual delineations from two experts using various assessment metrics. The experiment results confirm the efficacy and stability of the proposed method, and also indicate that the proposed method can be potentially used as a convenient BAC measurement tool in replacement of the trivial and tedious manual delineation tasks.

Index Terms—Breast arterial calcification (BAC), curve linking, mammography, uncertainty, vessel tracking.

I. INTRODUCTION

BREAST arterial calcification (BAC) is a phenomenon of calcium deposition along the vascular lumen in breast. In clinical mammographic screening, vessels with calcium depositions are often observed, but usually regarded as insignificant findings. Recently, BAC in mammography has been re-evaluated as a potential biomarker of women’s cardiovascular and coronary heart diseases [2]–[8]. Although the connection to cardiovascular and coronary heart diseases remains controversial [9], other relevant links to diseases such as bone mineral

density reduction [10], chronic kidney diseases [11], diabetes [7], [12], hypertension [12], vertebral fracture [13], and even breast cancer [14], are also continuously being investigated with positive conclusions. Accordingly, BAC as a biomarker for women’s cardiac and other chronic diseases has become an emerging research topic in recent years.

In previous studies [2]–[7], [9], [10], [12], BAC was mostly treated as a binary variable. That is, the specification of either present or absent is the only scoring factor of BAC in the statistical analysis. Few studies have investigated for correlations between the severity of BAC and the factors of cardiovascular and other related diseases. Actually, the severity of BAC is an important variable to corroborate the biomarker hypothesis, as it may support more insightful factor analysis by quantitatively describing BAC with a multilevel variable. This can be easily justified if one can conceive that vessels with severe calcium depositions may indicate far different health conditions from the cases with sparse calcium depositions. Therefore, the investigation of the correlation between BAC severity and degree of disease risk could be valuable and informative for further substantiation of the biomarker hypothesis.

To this end, we need to compute several quantitative measurements for evaluation of BAC severity, including the number of vessels with calcium depositions, vessel length and diameter, calcification density, and so on. The calculation of these measurements requires the accurate identification of calcified vessels in mammography. Since manual delineation is not efficient and could be subjective, we propose to develop in this paper a computerized BAC detection algorithm, for obtaining less-user-intervened and objective measurements.

A. Problem Description

Developing a computerized BAC detection algorithm for digital mammography is not a trivial task, since many difficult issues, which can be summarized into two major aspects, need to be resolved. **The first aspect of difficulty** is the less-uniform intensity distribution and appearance pattern in the vessels with calcium depositions. In mammograms, lumens of calcified vessels are expected to show relatively high intensity values due to significant X-ray attenuation. However, since breast density is highly subject-dependent, the X-ray attenuation of calcification may not be consistent across different subjects. Even for the same subject, different 2-D projection views may lead to different calcification distributions and different spatial appearance patterns. As indicated by yellow arrows in Fig. 1, vascular calcium may deposit in diverse patterns along vessels. Generally speaking, breast vascular calcifications can be in the form of

Manuscript received June 18, 2012; revised August 16, 2012; accepted August 19, 2012. Date of publication September 04, 2012; date of current version October 26, 2012. This work was supported in part by the National Institutes of Health under Grant CA140413, the GE Healthcare under Grant CA140841, and the National Basic Research Program of China (973 Program) under Grant 2010CB732505. Asterisk indicates corresponding author.

J.-Z. Cheng and C.-M. Chen are with the Institute of Biomedical Engineering, National Taiwan University, Taipei 100, Taiwan (e-mail: jzcheng@ntu.edu.tw; chung@ntu.edu.tw).

E. B. Cole and E. D. Pisano are with the Department of Radiology and Radiological Science, Medical University of South Carolina, Charleston, SC 29425 USA (e-mail: coleeb@musc.edu; pisanoe@musc.edu).

*D. Shen is with the Department of Radiology and Biomedical Research Imaging Center (BRIC), University of North Carolina, Chapel Hill, NC 27559 USA (e-mail: dinggang_shen@med.unc.edu).

Color versions of one or more of the figures in this paper are available online at <http://ieeexplore.ieee.org>.

Digital Object Identifier 10.1109/TMI.2012.2215880

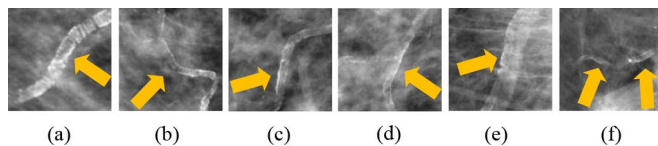


Fig. 1. Various appearance patterns of vessel calcifications, due to different amounts of calcium deposition and 2-D projection effects. Vessel calcifications are indicated by yellow arrows in (a)–(f).

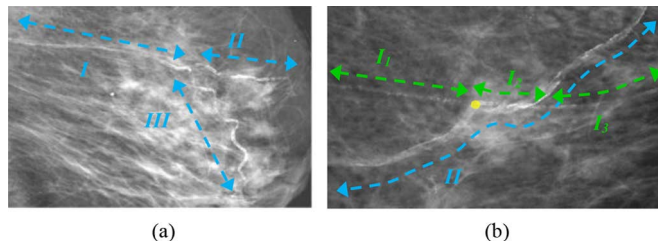


Fig. 2. Illustration on topological complexity and variation of calcified vessels. (a) A calcified vessel network with three branches (indicated by blue arrows). Branch *I* appear to be disconnected and hard to perceive, while branches *II* and *III* are relatively discernible. (b) Two twisted calcified vessels *I* (with three segments *I*₁, *I*₂, and *I*₃ as indicated by three green arrows) and *II* (marked by blue arrows).

bright tubular structures [cf. Fig. 1(a)], single or parallel linear (bright railway) structures [cf. Fig. 1(b)–(d)], and tubes with sporadic bright spots along wall and interiors [cf. Fig. 1(e) and (f)]. In these cases, the vessel intensity seems not a helpful feature for BAC detection.

The second aspect of difficulty is the topological complexity of calcified vessel structures in the breast. In the 2-D projection views, vessels may cross or overlap each other. Also, vessels can branch into a complicated network, and thus no general rule can be used to model their topology. In the other case, if one vessel comes in-and-out perpendicularly to the 2-D projection plane or happens to be occluded by other breast tissues, this vessel may appear disconnected in the mammogram. Thus, difficulty of detection may increase. Fig. 2 provides several examples. Specifically, Fig. 2(b) shows a difficult case where two vessels with different diameters, denoted as *I* and *II*, are twisted together. In vessel *I*, its segment *I*₂ is separated from its segment *I*₁ with a perceivable gap, and also overlaps with vessel *II*. This will confound the extraction process, especially around the location of the yellow point. If the vessel calcification extraction process is performed along the vessel *II*, it will probably go along the lower-left direction around the yellow point. However, when it is performed along the vessel *I*, it may be terminated at the yellow point. As a result, the vessel calcification extraction process needs to address not only the vessel extraction problem, but also the disconnection issue very carefully.

The vessel tracking and segmentation problems have been extensively studied in 3-D [15]–[21] and 2-D [22], [23] images. As indicated in [21], the related methods can be categorized as ridge tracking [17], [22], tubular tracking [16], [24], cross-section tracking [19], [20], front propagation [18], [25], [26], and region growing. Another more thorough review can also be found in [27]. In brief, the ridge tracking methods [17], [22] commonly perform eigen-analysis on the computed Hessian

matrix to locate the center of vessel in single solution. The ridge tracking methods may have trouble in dealing with the vessel branching and overlapping problems, and thus require extra handling. Tubular [16], [24] and cross-section tracking [19], [20] methods either assume the continuity of lumen size by using tubular shape prior, or model the lumen with ellipses in the probabilistic framework. The front propagation methods [18], [25], [26], or more generally the deformable models [26], [28], often need to incorporate the vessel shape as prior to regularize the evolution of the deformable model. Note that the tubular and cross-section tracking methods, as well as deformable models, assume that the vessel shape does not change abruptly. However, as shown in Figs. 1 and 2, the shape/diameter of calcified vessel may change suddenly. Therefore, the vessel shape is not a useful clue in our targeted problem. On the other hand, the vessel tracking and segmentation for carotid and coronary arteries [15], [19]–[21], [24] may also encounter similar issue of irregular lumen appearance (lumen + calcification). Note that, in mammography, the appearance of calcified vessel may have more complicated composition (lumen + calcification + other tissues) due to 2-D projection effect. Therefore, the problem here is to identify multiple vessels with different size and irregular appearance, and to address vessel disconnection issue. This problem is not well addressed with previous vessel tracking methods.

B. Related Works

Computerized detection of calcified vessels in mammograms is a relatively new research topic. In the literature, there are few relevant studies. Ge *et al.* [29] developed a detection method based on calcification clues only [1], [30], [31]. Specifically, a principal curve clustering technique was first developed to identify the regression curves from the point cloud of calcification cues. Then, a classifier was further used to reduce the false positives. Their approach was capable of detecting some calcified vessel “segments,” but not the complete vessel tract and the highly-winding vessels. This could be an issue when reporting the calcification severity measures, such as the length of each individual vessel tract and the number of calcified vessels.

In this study, we leverage both calcification and vesselness cues into an integrated framework, for detection of vessels with calcium depositions from the digital mammography. First, calcifications in mammograms are identified from other normal tissues, and a vesselness filter [32] is applied to narrow down the search space from the complex tissue composition to tubular structures. Then, we use these identified calcification cues to initialize our new tracking with uncertainty scheme, along with help of vesselness [32], to generate multiple sampling paths for tracking the calcified vessels, which has been shown effective in fiber tracking [33]–[35], sulci detection [36], and 4D blood flow tracking [37], [38]. Finally, we use a new compiling and linking process to reconstruct the vessel structures.

The major contribution of this paper is threefold. First, a new vessel tracking with uncertainty scheme and the latter compiling and linking process are introduced to delineate calcified vessels with complex topology in the mammogram. Second, a linear structure analysis technique is developed for reliable detection of calcification cues. Third, we conduct a pioneering study on

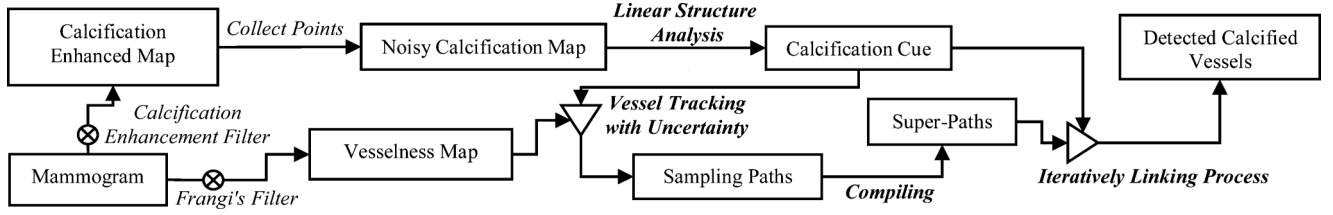


Fig. 3. Diagram of the proposed method.

applying our method to calcified vessel identification in mammography, for meeting the need of emergent BAC biomarker research. The experimental results show that our method can produce results comparable to well-trained manual raters.

II. METHOD

The proposed method is composed of four major steps. In the first step, reliable calcification cues are computed with the proposed linear structure analysis method (Section II-A). The second step calculates the vesselness cues [32](Section II-B). With the two computed underlying calcification and vesselness cues, the vessel tracking with uncertainty scheme is then employed to generate multiple sampling paths for tracking the calcified vessels in mammography (Section II-B). The final step performs the compiling and linking process to obtain the final result (Section II-C). Fig. 3 gives a diagram of the proposed method.

A. Calcification Cue With Linear Structure Analysis

In a mammogram, vessels with calcium deposition may appear like bright-railway structures, as shown in Fig. 1(b) and (c). Compared to other appearance patterns [Fig. 1(e)], this kind of bright-parallel-linear pattern can be more certainly labeled as parts of calcified vessels. Accordingly, it will be helpful if we can identify them first in the mammogram. To this end, we first use the technique in [1] to collect a number of calcification candidate points. Subsequently, a parallel linear structure detector is carried out to locate those calcification points with bright-parallel-linear patterns. Because those identified points can be parts of the vascular calcium depositions with high confidence, we are able to estimate the distribution of the true vascular calcium depositions in a feature space. With knowledge of this feature distribution, we can specifically define a range to reject points beyond the estimated range.

On the other hand, some calcification points may constitute as a single linear structure, as demonstrated in Fig. 1(d) and (e). To identify this type of calcium depositions and rule out more false calcifications, a single-linear structure detector is further applied.

1) *Detection of Calcification Candidates*: The calcification points are detected by using a technique in [1]. The basic idea is to first enhance the calcification signals by computing the difference of two filtered images, $F = F_e - F_r$. Here, F_e is a filtered image with a low-pass filter. F_r is obtained by convolving the mammogram with a calcification signal suppression filter: $f = [2f_A - 1]f_B$, where f_A is a low-pass smoothing filter and f_B is a high-frequency noise-suppressing filter. Specifically, in

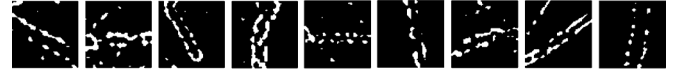


Fig. 4. Vessel calcifications, centered Regions of Interest (ROIs), appear as parallel linear structures (with various orientations and calcium deposition patterns) in calcification map.

this study, f_A is selected as a Gaussian kernel filter with standard deviation of 4.5 (in pixels), and f_B as a mean filter. Then, a global thresholding is applied to collect at most N_{cal} highest response points in the enhanced difference image F , as the detected calcifications. This can be achieved by finding the minimal threshold ϖ^* that makes the number of the thresholded points no larger than N_{cal}

$$\{p_{\varpi^*}\} = \min_{\varpi} \{p | p \in F, F(p) \geq \varpi, \text{s.t. } \|\{p\}\| \leq N_{cal}\} \quad (1)$$

where $\{p_{\varpi^*}\}$ is the point set of the collected calcification candidates, ϖ is an intensity threshold, and N_{cal} is set empirically to 8000 in this paper.

2) *Detection of Parallel Linear Structure Patterns*: In the 2-D calcification map built with those detected calcification points $\{p_{\varpi^*}\}$, the bright railways appear as parallel linear structure patterns. The desired parallel linear structures may be oriented in various directions and usually appear disconnected due to sporadic calcium deposition. Meanwhile, other false-detected calcifications may also present (cf. Fig. 4). Hence, the detector for parallel linear structures should be invariant to the vessel orientations and also robust to sporadic calcium deposition. To this end, the parallel linear structures will be detected by the following two steps: 1) local orientation estimation and projection profile generation, and 2) projection profile analysis along the estimated local orientation. Fig. 5 demonstrates the whole process of projection profile analysis for the parallel linear structures in calcification map. More details of these two steps are provided below.

Local Orientation Estimation. To obtain the right projection profile for analysis, the orientation of the local structure should be first estimated. Given a local window, W_p , of the calcification map centered at the centroid p of the current connected component, the local orientation v_p can be estimated by: $v_p = \arg_v \max W_P \circ L_{v,0}$, where $W_P \circ L_{v,0}$ is the integration of W_P along the line function $L_{v,0}$ parameterized by the angle v and zero distance offset from the center of the local window. An integral line function $L_{v,\gamma}(x, y)$ with angle v and distance offset γ is defined as $x \cos v + y \sin v + \gamma$. The local window W_p is a circular region with radius of 25 (pixel). For robustness, the local orientation of the current connected component will be

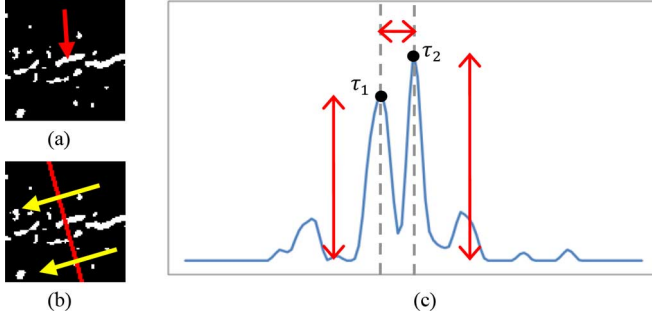


Fig. 5. Illustration of projection profile analysis of the calcification cluster indicated by the red arrow in (a). (a) ROI of a calcification map. (b) projection of spatial calcification distribution. (c) the obtained projection profile after smoothing. In (b), the yellow arrows indicate the estimated local orientation. In (c), τ_1 and τ_2 are the two strongest peaks near the center of the profile. Red arrows indicate the magnitudes of τ_1 and τ_2 , and the distance between τ_1 and τ_2 , respectively. In this case, the calcification cluster is part of parallel linear structure.

averaged with other estimated local orientations in the neighboring connected components. The projection profile along the estimated v_p can be obtained by computing $W_p \circ L_{v_p, \gamma}$ with varying distance offset γ along the direction perpendicular to v_p , e.g., along the red line for the case in Fig. 5. The search space ranges from 0° to 179° with discretization of 3° , along with discretization of γ as 1(pixel).

Projection Profile Analysis. The 1-D projection profile of a parallel linear structure along the local orientation is expected to have dual strong peaks near the center of the profile; see Fig. 5(c) for example. The peaks in a profile can be identified by 1-D watershed transformation [39]. Then, we seek the two strongest peaks near to the center of profile such as τ_1 and τ_2 in Fig. 5(c). If both peaks, τ_1 and τ_2 , are stronger than a given threshold, δ_s , and the distance between the two peaks is within a specific distance, denoted as δ_d , the profile is considered having dual strong peaks. If the projection profile possesses the dual strong peaks around the center, the current tested connected component will be regarded as a part of one parallel linear structure. The two thresholds, δ_s and δ_d , are learnt from a set of manually-labeled samples of parallel linear structures, as will be detailed in the experiment section.

The parallel linear structure detector finally selects a subset $\{p_{\varpi}^l\}$ from the point set $\{p_{\varpi}^*\}$ as calcification candidates with bright railway patterns. The point subset $\{p_{\varpi}^l\}$ can help us to exclude those points which are far different from the true calcifications. Recalling that the feature image, F , is the filtered result with the calcification enhancement filter, we are able to calculate the mean μ_{ϖ}^l and standard deviation σ_{ϖ}^l of the parallel linear structures from the feature set $\{F(p_{\varpi}^l)\}$. With these statistics, we can discard any point p_{ϖ}^d in $\{p_{\varpi}^*\}$ which satisfies $F(p_{\varpi}^d) < \mu_{\varpi}^l - \alpha_{\text{dic}} \sigma_{\varpi}^l$. Here, α_{dic} is a discarding factor that is set as 1.0 in our study. After performing the exclusion process, we have a set of the candidate calcification points $\{p_{\varpi}^e\} = \{p_{\varpi}^*\} - \{p_{\varpi}^d\}$.

3) *Consideration of Single Linear Structures:* Some calcifications may appear like a single line, instead of railway. We are also interested in identifying them, which can be denoted as p_{ϖ}^s . This identification process is similar to the task of finding

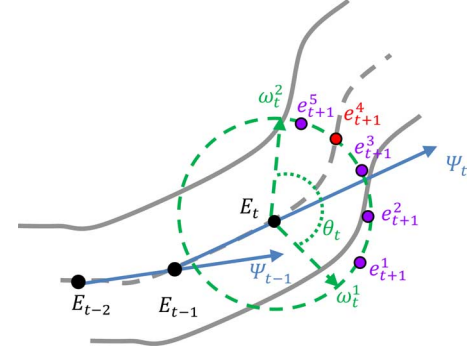


Fig. 6. The configuration of search window. Bold grey curves represent the vessel boundaries, and the dashed grey curve in the middle denotes the medial axis of the vessel. Solid blue arrow Ψ_t indicates the traversing direction, and a black solid point E_t is the current TEP. The search window is defined by two dash green arrows ($\overline{E_t \omega_t^1}$ and $\overline{E_t \omega_t^2}$ and arc ω_t^2 of angle θ_t). The points, e_{t+1}^j , $1 \leq j \leq 5$, are the candidate points for next TEP E_{t+1} , while e_{t+1}^4 is regarded as E_{t+1} in this case.

parallel linear structures in $\{p_{\varpi}^*\}$, but only one peak is considered in the current case. As the locations of the parallel linear structures have already been known, we can only find those single linear structures in the set $\{p_{\varpi}^{e-l}\} = \{p_{\varpi}^e\} - \{\{p_{\varpi}^e\} \cap \{p_{\varpi}^l\}\}$. We select the points in the set $\{p_{\varpi}^{e-l}\}$ which hold a single peak strength larger than β_{sig} in the projection profile, and denote the collected point set of single linear structures as $\{p_{\varpi}^s\}$. Distinct from the parallel linear structure detector, the parameter β_{sig} is empirically set as 8.0 as it is less important in the whole process of linear structure analysis. We output the joint calcification point set $\{p_{\varpi}^o\} = \{p_{\varpi}^s\} \cup \{\{p_{\varpi}^e\} \cap \{p_{\varpi}^l\}\}$ as the candidate set of vascular calcium depositions.

B. Vessel Tracking With Uncertainty

The vesselness probability map for tracking is generated by Frangi's vesselness filter [32]. The vesselness filter [32] consists of two exponential functions, which describe "the second order structureness" and "the tube-like structure," respectively, and is computed at different scales. Three scales for the standard deviation, i.e., 2, 5, and 8 (pixel), are applied here. The final response of Frangi's filter is determined by the maximum in the scale space. More details can be found in [32]. We denote the computed vesselness of each pixel q as $\mathcal{V}(q)$.

A standard vessel tracking algorithm is commonly designed to delineate a tract of interest by iteratively finding next candidate tracking element point (TEP) [17]. Basically, the determination of next TEP can be influenced by three major tracking factors, i.e., *traversing direction*, *search distance*, and *vesselness* value. Traversing direction and search distance configure the search window, which delimits the search area of the next TEP. The traversing direction specifies the projection direction of the search window, while the search distance suggests how far to search the next candidate points in the neighborhood.

The search window can be defined as a fan shape near the area projected from the current TEP. The configuration of the search window is presented in Fig. 6, where the radius of the dashed green circle represents the search distance. The fan-shape search window at the current TEP E_t is spanned along the traversing

direction Ψ_t with an angle θ_t . To avoid back tracking, the spanning angle θ_t is usually expected to be smaller than 180° . The next TEP E_{t+1} can be selected from a pool of candidate points, e.g., $e_{t+1}^j, 1 \leq j \leq n_e^t$, according to the vesselness values. n_e^t indicates the number of candidate points within the search window spanned from TEP E_t . The selection criteria for the next TEP can be simply to choose the candidate point with the largest vesselness value. For example, the local maximum was always selected as next TEP in the study [17].

In mathematical formulation, a simple vessel tracking process can be described as a system of the above two variables TEP E_t and traversing direction Ψ_t

$$E_{t+1} = E_t + \alpha_t \Psi_t + d_t^{\theta_t, \mathcal{V}} \quad (2)$$

$$\Psi_{t+1} = \Psi_t + \kappa_t (\varphi_{t+1} - \Psi_t). \quad (3)$$

In (2), α_t is regarded as a search distance for the next TEP E_{t+1} , and $d_t^{\theta_t, \mathcal{V}}$ is the offset of the selected next TEP E_{t+1} relative to the linear prediction $E_t + \alpha_t \Psi_t$. It may be worth noting that the offset $d_t^{\theta_t, \mathcal{V}}$ depends on the spanning angle θ_t and vesselness measure \mathcal{V} of a TEP candidate. Meanwhile, the estimation of the offset $d_t^{\theta_t, \mathcal{V}}$ may sometimes not be a linear process. Variable φ_{t+1} in (3) is the current traversing direction measurement and can be calculated as $E_{t+1} - E_t$, while κ_t is a blending factor. In every iteration, the norm of new traversing direction Ψ_{t+1} should be normalized to 1.

1) *Our Vessel Tracking Algorithm*: We explore uncertainties in the three tracking factors with Monte Carlo method. Specifically, we treat the uncertainty of each tracking factor with a uniformly distributed random variable and then generate a number of sampling paths for calcified vessels. At each iteration, the tracking process stochastically picks next TEP with random perturbation of the variables with respect to the three tracking factors. At the termination of a tracking process, one sampling path of a seeding point can be obtained. For the spanning angle θ_t , we leave it as a predefined constant value 90° . The purpose of sampling the paths for calcified vessels is to identify as many solutions as possible. The handling of wrong sampling paths is deferred to the latter process. The issue of setting the sampling path number will be discussed in the experiment section.

Seeding Strategy and Initialization. As shown in Section II-A, the seeding points used for the vessel tracking process with uncertainty are obtained from the output of the linear structure analysis, i.e., points in the set $\{p_{\varpi}^o\}$. We first conduct the connected component analysis on the point set $\{p_{\varpi}^o\}$ and select the point in a connected component with the highest vesselness value as an initial seeding point. To do better seeding, we acquire more than one initial seed in the large connected components. For each seed, we render N_{samp} sampling paths to delineate vessel tracts of interest. Because the seeding point may not locate at the center of vessel [see the yellow dot in Fig. 7(a)], we apply principle component analysis (PCA) to analyze the spatial distribution of vesselness in the vicinity of the seeding point. The derived eigenvector with higher magnitude of eigenvalue is taken as an initial traversing direction $\pm \Psi_0$ [i.e., the longer red line in Fig. 7(a)], for forward and backward tracking. Along the other eigenvector, i.e., the shorter red line in Fig. 7(a), a seeding point can be relocated

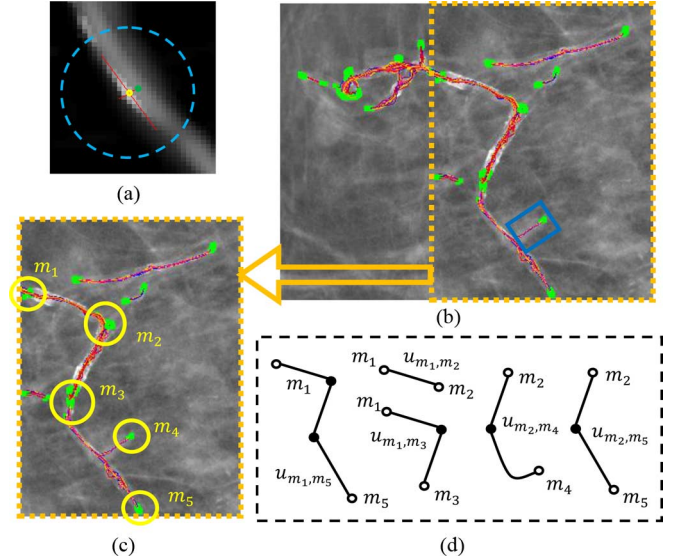


Fig. 7. (a) Relocation of a seeding point towards the center of a vessel. Blue dashed circle denotes the vicinity of the original seeding point, marked as a yellow dot in the figure. The green dot is the relocated position of the seeding point. Red crossed lines represent the two eigenvectors of PCA on the local vesselness map. (b) An example of generated sampling paths on a selected part of mammogram. The green dots denote the ending points of sampling paths. The blue rectangle in (b) indicates a wrongly-tracked path. (c), (d) Illustration the concept of compiling the sampling paths into super-paths. There are five clusters of ending points that are identified by yellow circles in (c). Five corresponding super-paths defined by the five clusters of ending points in (c) are depicted in (d).

approximately toward the center of vessel, e.g., the green dot in Fig. 7(a). The relocated seeding point is the initial TEP E_0 . One example of the tracked sampling paths is depicted in Fig. 7(b).

Traversing Direction. The traversing direction specifies the direction of current tracking. Here, we simply model the traversing direction with the (3). The blending factor κ_t can be treated as a confidence weighting between the tracking model and the current estimation, similar to Kalman gain in Kalman filter. Since we do not have knowledge about the accuracy of the current estimation, the blending factor is *uncertain*. Instead of elaborating on calculation of the blending factor, we treat this blending factor κ_t as a uniformly distributed random variable, ranging from 0 to 1.

Search Distance. The search distance, such as the variable α_t in the (2), is the factor that defines how far to find a desired next TEP E_{t+1} . There is no general setting to assert whether a smaller or larger search distance is more likely to lead to undesired tracking course or premature termination. We describe the uncertainty of the search distance α_t with another uniformly distributed random variable, which ranges from 6 to 10 in pixel unit.

Selection of TEP with Vesselness Cue. With the information of traversing direction Ψ_t and search distance α_t , we can do a prediction of the next TEP \hat{E}_{t+1} by simply computing $E_t + \alpha_t \Psi_t$. Based on the predefined spanning angle θ_t of the current search window and the precomputed vesselness cue, we are able to select the desired next TEP E_{t+1} within a specific range; see Fig. 6. A good pick of next TEP E_{t+1} is also crucial to keep a tracking pass staying in the right trajectory. As indicated before, the vesselness within the vessel tract or the vicinity cannot be

guaranteed to be the local maxima, and multiple local maxima may exist within the search window. In this circumstance, it is very difficult to assess the candidates. Here, we turn to a random selection process to pick the next TEP E_{t+1} from the range defined by the current search window. The candidates of TEP E_{t+1} are selected by vesselness cue as follows:

$$\begin{aligned} \{e_{t+1}^j\} &= \arg \max_{p_{t+1}^w} \mathcal{V}(p_{t+1}^w) \\ \forall j, 1 \leq j \leq n^s \text{ and } \forall p_{t+1}^w \in \mathcal{W} \end{aligned} \quad (4)$$

where \mathcal{W} is the region of interest within the fan-shaped search window. Here, \mathcal{W} is defined as a ring region dilated from the periphery of the fan-shape search window with thickness in 2 pixels (i.e., the dashed circle in Fig. 6). n^s is the number of candidates to be selected, and is set as 10 in this paper. Since there is no sufficient knowledge about which candidate is more proper to be the next TEP E_{t+1} , a candidate is randomly picked as E_{t+1} from the set $\{e_{t+1}^j\}$, $1 \leq j \leq n^s$.

Termination of Tracking Scheme. The vessel tracking process with uncertainty iterates until no strong vesselness in the current TEP. We introduce a vesselness threshold π_{tm} to control the termination of a tracking pass. Specifically, when no candidate points, $\{e_{t+1}^j\}$, of TEP E_{t+1} satisfies $\mathcal{V}(e_{t+1}^j) \geq \pi_{tm}$, the current tracking process will be terminated.

Because the distribution of vessels may be highly image-dependent, the determination of π_{tm} could be difficult. To this end, we utilize Otsu's thresholding technique [40] to bipartition the vesselness into valid and invalid groups with threshold π_{tm}^* . However, as the common problem shared by many thresholding schemes, there are cases where the vesselness distributions are not bi-modal. In those cases, Otsu's technique may fail to propose a useful π_{tm}^* . To compensate this drawback, we blend the obtained optimal π_{tm}^* with an empirical value 0.1 and have the final vesselness threshold as $1/2(\pi_{tm}^* + 0.1)$.

C. Compiling and Linking of Sampling Paths

The multiple-seeded vessel tracking scheme with uncertainty generates many sampling paths and thus requires a postprocessing step to determine the desired sampling paths. In this section, we cast the postprocessing step as a compiling and iteratively linking process. As many sampling paths drawn from the distinct seeding points may correlate each other in some degrees, it may be reasonable to group the correlated sampling paths into a "super-path." Motivated by this, a compiling process is developed to parcel up the sampling paths (with close ending points in both ends) into sets of super-paths. The latter linking process of the super-paths is carried out in an iterative fashion to link up the super-paths: a gradually stricter constraint is iteratively applied in the linkage establishment of more distant pairs of super-paths. Meanwhile, ineligible super-paths are discarded gradually. The iterative linking process will not terminate until no more linkage can be established.

1) *Compiling the Sampling Paths Into Super-paths:* To facilitate the linking processing, the sampling paths are further compiled into sets of super-paths. A super-path is defined as a bundle of the sampling paths that have close ending points in both ends, see Fig. 7(c) and (d). To this purpose, the ending points of all sampling paths are clustered with L_2 (Euclidean)

distance metric first, by grouping points within five pixels together. All sampling paths sharing the same pair of clusters of ending points are compiled into the same super-path. As shown in Fig. 7(c), the close ending points are aggregated into five clusters, i.e., m_1 , m_2 , m_3 , m_4 , and m_5 . Fig. 7(d) lists five corresponding super-paths defined by the two ending clusters. It may be worth noting that the super-paths u_{m_1, m_2} , u_{m_1, m_3} , u_{m_2, m_5} are regarded as incomplete paths with respect to the super-path u_{m_1, m_5} . Super-path u_{m_2, m_4} is counted as a wrongly-tracked path, as the path portion ended at cluster m_4 is not a calcified vessel.

After compilation, a few representatives of a super-path are picked from the member sampling paths of each super-path, to facilitate the successive steps. The selection of representatives is to scale down the number of paths, while the reason of choosing more than one representative is to achieve robustness to the noisy tracking results. A representative member sampling path is picked if it appears to be smoother than other member paths. Here, we use curvature to quantify the smoothness of a sampling path. For each super-path u_i we select $\max(1, N^{u_i}/4)$ paths from its member sampling paths as representatives. Here N^{u_i} stands for the total number of member sampling paths in super-path N^{u_i} . Having representatives of every super-path, we are able to compute unary features of each super-path and pairwise features for the interrelation between super-paths.

2) *Discarding Ineligible Super-Paths:* The derived sampling paths may have some paths without calcification, and also the incomplete or wrongly-tracked paths. Generally, an incomplete path is ended prematurely at the middle of a calcified vessel, whereas a wrongly-tracked path is partially ended at a locus which is not part of a calcified vessel. For these two kinds of paths, we may compute the overlapping ratio between paths for identification, since an incomplete or wrongly-tracked path may share its major portion with the complete path. However, only counting the overlapping ratio may not provide a satisfactory elimination result, since the tracts of a branching vessel may also hold the high overlapping ratio in some cases. Accordingly, we defer the problem of eliminating the incomplete and wrongly-tracked paths to the linking step, as it may require the linking cue to fulfill the elimination job.

On the other hand, although the linear structure analysis in Section II-A can eliminate most false calcifications, there may still exist a small amount of false calcifications, which will lead to the detection of noncalcified vessels and also affect the latter linking step. Therefore, this kind of noncalcified vessels should be removed. To do this, we compute a unary feature, i.e., calcification density, for every super-path, and then discard the super-paths with calcification densities lower than a certain threshold c_{den} . Here, c_{den} is empirically set to 0.005, which is determined by conducting a linear search to find a best separation of 100 training calcified and noncalcified vessel segments within the 1-D feature space of calcification density. The value 0.005 is a conservative threshold, as we may see the lowest calcification density as ~ 0.01 in Fig. 14. Extremely short paths, i.e., less than 10 pixels, are regarded as trivial tracking results and thus discarded.

3) *Iterative Process for Linking up the Super-Paths:* Two major tasks are carried out in the linking process: 1) linking up

the super-paths that belong to the same vessel, and 2) discarding the incomplete and wrongly-tracked super-paths. The two tasks require the implementation of the three pairwise features: overlapping ratio, linking cue, and distance measure. For robustness, the pairwise features of super-paths u_i and u_j , except the linking cue, are averaged over every matching pair of the representatives in the two super-paths. The linking cue is computed with the concept of curvilinear continuity. Curvilinear continuity is the contextual cue for mid-level inference in human visual perception [41]. As suggested in [41], the curvilinear continuity can be measured by turning angle (see Fig. 9). Thus, we take the turning angle as our linking cue. In this study, we use the distance measure for the proximity between the two super-paths.

The overlapping ratio is asymmetric. Specifically, the overlapping ratio from path A to path B is defined as $len(A \cap B)/len(A)$, where $len(A \cap B)$ is the length of intersection portion and $len(A)$ is the length of path A . Similarly, the overlapping ratio from path B to path A can be computed as $len(A \cap B)/len(B)$. For simple illustration, in Fig. 7(d), super-path u_{m_1, m_2} is an incomplete path to the super-path u_{m_1, m_5} , and hence the overlapping ratio from u_{m_1, m_2} to u_{m_1, m_5} is much larger than the ratio from u_{m_1, m_5} to u_{m_1, m_2} . The linkage establishment between a pair of super-paths is based on the linking cue and proximity. Proximal super-paths may deserve a looser linking constraint, whereas the linkage between distant super-paths should be constrained by stricter turning angle value. Accordingly, we introduce an iteration index, i.e., distance scale d , in the process of linkage establishment. At the lower distance scale, i.e., in the case where the super-paths are close to each other within a given distance threshold, a looser angle constraint is applied. When the distance scale goes higher and the distant super-paths are considered, a more rigorous angle constraint is employed.

The iterative linking process is formulated in an algorithmic graph construction. Fig. 8 summarizes the linking process with pseudo-codes. At each distance scale d , a linking graph $G_d = \{U^d, X^d\}$ is constructed by setting each super-path as a graph node, u_i^d , where U^d is the set of all graph nodes and X^d is the set of all linkage can be established. The pairwise features, linking cue $\rho_{i,j}^d$ and distance measure $\ell_{i,j}^d$, are computed for the linkage (graph edge) establishment at distance scale d . The graph edge $x_{i,j}^d$ is established if the distance and angle conditions, $\ell_{i,j}^d \leq L^d$ and $\rho_{i,j}^d \leq \Theta^d$, are satisfied. Denoting that L^d and Θ^d are the distance and angle thresholds of the current distance scale d , respectively, the distance between super-paths u_i^d and u_j^d , denoted as $\ell_{i,j}^d$, is calculated as

$$\ell_{i,j}^d = \frac{1}{p_i \times q_j} \sum_{r=1}^{p_i} \sum_{s=1}^{q_j} dist(\zeta_r^i, \zeta_s^j) \quad (5)$$

where p_i and q_j are the respective numbers of representatives within the super-paths u_i^d and u_j^d , and ζ_r^i and ζ_s^j stand for the representatives with respect to super-paths u_i^d and u_j^d . The function $dist(\zeta_r^i, \zeta_s^j)$ is the L_2 distance between the two connecting ending points of ζ_r^i and ζ_s^j . The turning angle between super-paths u_i^d and u_j^d , $\rho_{i,j}^d$, is determined via selecting the minimum of turning angles in all possible matching pairs of representatives ζ_r^i and ζ_s^j : $\rho_{i,j}^d = \min_{\zeta_r^i, \zeta_s^j} \vartheta(\zeta_r^i, \zeta_s^j)$. The function $\vartheta(\zeta_r^i, \zeta_s^j)$

1. *Iteratively Linking Process*
- 2.
3. Pick representatives for each super-path after elimination of ineligible super-paths
4. Initialize constraints: $O_{incm}^0, O_{cm}^0, O_{wt}^0, O_{good}^0, L^0, \Theta^0, \varepsilon^0$ and set $d = 0$
5. Treat current survival super-paths as graph nodes, u_i^d
6. do
7. for all pairs of u_i^d and u_j^d
8. Compute distance and angle features: $\ell_{i,j}^d$ and $\rho_{i,j}^d$
9. Establish linkage, $x_{i,j}^d$, when conditions $\ell_{i,j}^d \leq L^d$ and $\rho_{i,j}^d \leq \Theta^d$ are satisfied
10. end
11. Linking graph G_d is constructed
12. Identify every connected component C_k^d in the link graph G_d
13. for those connected component C_k^d with only one graph node u_k^d
14. Compute overlapping features of u_k^d with other graph node u_j^d : $o_{k,j}^d$ and $o_{j,k}^d$
15. if u_k^d satisfies conditions $o_{k,j}^d \geq O_{incm}^d$ and $o_{j,k}^d < O_{cm}^d$
16. Discard u_k^d (incomplete super-path)
17. else if u_k^d satisfies conditions $o_{k,j}^d \geq O_{wt}^d$ and $o_{j,k}^d < O_{good}^d$
18. if u_k^d has at least one ending part with averaged calcification density $< c_{den}$
19. Discard u_k^d (wrongly-tracked super-path)
20. end
21. else if $len(u_k^d) < \varepsilon^d$ && $den(u_k^d) < c_{den}$
22. Discard u_k^d
23. end
24. end
25. $O_{wt}^{d+1} = O_{wt}^d$; $O_{good}^{d+1} = O_{good}^d$; $O_{incm}^{d+1} = O_{incm}^d$; $O_{cm}^{d+1} = O_{cm}^d$; $\varepsilon^{d+1} = \varepsilon^d + \Delta\varepsilon$
26. $L^{d+1} = L^d + \Delta L$; $\Theta^{d+1} = \Theta^d - \Delta\Theta$; $d = d + 1$
27. Convert all survival connected component C_i^{d-1} as u_i^d
28. Compile sampling paths for each u_i^d
29. Pick representatives for each u_i^d
30. while there is at least one linkage establishment

Fig. 8. Summary of iterative linking process. Here, “ $len(u_k^d)^n$ ” indicates the averaged length of all representatives of u_k^d , and “ $den(u_k^d)^n$ ” denotes the averaged calcification density of all representatives of u_k^d .

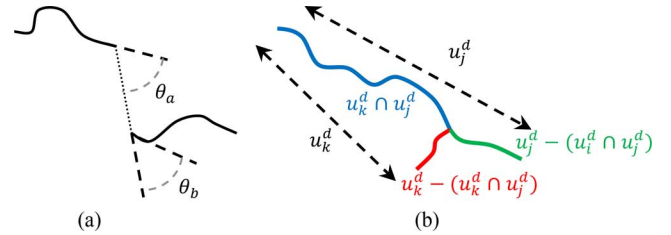


Fig. 9. (a) An illustration of turning angle. The two solid curves are the two sampling paths, and the dotted line is the gap-filling line. The turning angle can be calculated as $\theta_a + \theta_b$. θ_a and θ_b are the angles between the tangents of the connecting ending points of u_a and u_b and the linkage line, respectively. (b) Assuming that u_k^d is a wrongly-tracked super-path and u_j^d is a normal one, the ending part of u_k^d is the red segment.

indicates the turning angle between the representatives ζ_r^i and ζ_s^j after the corresponding linkage is established; see Fig. 9(a) for concept illustration. For the update of linkage establishment constraints, the variables ΔL and $\Delta\Theta$ are assumed to be related. Let $z = \Delta\Theta/\Delta L$, the update of Θ^d to higher scale $d + 1$ can then be related to the update of L^d , as $\Theta^{d+1} = \Theta^d - z\Delta L$. In the experiment, we will discuss the effect of choosing of z to the overall detection performance. The initial linking constraints, L^0 and Θ^0 , are suggested to be set as 80 (pixel) and 60° , respectively. Lines 7–10 in Fig. 8 summarize the linkage establishment.

After graph construction, the linking graph G_d is a forest of several connected components, which can be found by depth-first search technique. A connected component here is composed of at least one super-path. If a connected component is constituted of two or more linked super-paths, it stands for a new path with several linkage establishments. Before moving

to next larger distance scale, some wrongly-tracked or incomplete super-paths, e.g., the super-paths u_{m_1, m_2} and u_{m_2, m_4} in Fig. 7(d), from those graph nodes without linkage establishment, i.e., the connected components composed of single graph node, are discarded. A wrongly-tracked or incomplete super-path is conservatively identified if it is not linked and holds high overlapping ratio with others. The wrongly-tracked or incomplete super-paths are discarded if the corresponding conditions described in Fig. 8 (Lines 15–20) are satisfied, respectively. In Fig. 8, O_{incm}^d is the lower bound of constraint specifying the overlapping degree of incomplete super-paths to the corresponding complete ones, while O_{cm}^d is the safe check to ensure that a branching super-path will not be discarded by accident. Similarly, O_{wt}^d is the lower bound for identifying a wrongly-tracked super-path, and O_{good}^d is the safe check. An extra condition is applied to further confirm a wrongly-checked path. We first find out an ending part, defined in Fig. 9(b), and compute the corresponding calcification density. If the density of the ending part is higher than the previous defined c_{den} , the current tested super-path may be regarded as a branching. Otherwise, current super-path will be discarded as wrongly-tracked. O_{wt}^d is expected to be smaller than O_{incm}^d , and the settings of O_{incm}^0 , O_{cm}^0 , O_{wt}^0 , and O_{good}^0 are recommended to be set as 0.95, 0.85, 0.85, and 0.85, respectively.

In addition to elimination of wrongly-tracked and incomplete super-paths, we also discard short isolated super-paths with low calcification density; see the statements of Lines 21–22 in Fig. 8. ε^0 and $\Delta\varepsilon$ are set as 10 and 5, respectively. With elimination of incomplete and wrongly-tracked super-paths, the linking process is proceeded to the next distance scale $d + 1$. All survived connected components in G_d are then converted as individual graph node at scale $d + 1$ (Lines 27–29 in Fig. 8). All linking and elimination constraints are also updated for next scale. The linking iteration will terminate when there is no linkage can be established anymore.

III. EXPERIMENTS AND RESULTS

The experiments are divided into two parts. The first part focuses on the issues of the major parameter determination in the linear structure analysis, vessel tracking, and linking process. The second part gives the overall performance evaluation of the proposed method. The performance analysis is conducted on 63 full-field digital mammograms, collected in N.C. Memorial Hospital, University of North Carolina at Chapel Hill. The pixel resolution of each digital mammogram is $0.05 \times 0.05 \text{ mm}^2$. To provide ground truth and account for inter-observer variation, manual identifications on the 63 mammograms from two experts are performed for evaluating computer-estimated results.

Three assessment metrics: difference of the total vessel length (Diff_Ln), length of missing segments (Miss_Ln), and length of false detected segments (FD_Ln) are calculated to illustrate the specific differences between computer-generated results and manual identifications from experts. The difference of the total vessel length (Diff_Ln) is measured by simply calculating the difference of the total lengths of vessels in the two sets under comparison. The missing segments are checked if they are missed in one set (R) but exist in other set (Q), when comparing the set R to the set Q . On the other hand, those

segments that exist in R but not in Q are regarded as false-detected segments. The total lengths of missing and false-detected segments in each testing mammogram are taken as Miss_Ln and FD_Ln metrics, respectively. The three assessment metrics are measured in millimeter (mm) for the table shown below.

Two vessel tracking methods: Aylward's method [17] and particle filter [19], [20], are also implemented as baseline methods for comparison. For fair comparison, both position transition and direction transition of a particle is performed similarly as ours. Specifically, for the position transition, one may interpret α_t as a random noise, and κ_t can also be regarded as a random noise for the direction transition. Samples of position and direction can be drawn with the perturbation of random noises α_t and κ_t , respectively. Also, sampling importance resampling (SIR) algorithm, as recommended by [19], [20], is adopted here to update the weightings of particles. Pruning of samples is further implemented to discard those particles with low weightings. The locations, where the Kullback–Leibler distances are large, are recorded and taken as terminations for the latter linking process. As shown earlier, the problem in our study is to detect multiple vessel tracts with various sizes and appearances, even for the cases with vessel disconnection. However, most vessel tracking algorithms in the literature, including these two selected baseline methods, were not designed to resolve such complicated problem. Therefore, these two baseline tracking algorithms need to be seeded with multiple calcifications to identify multiple calcified vessels. Also, to address the vessel disconnection issue, the results of these two baselines need to be compiled and linked by our method to get the final complete vessel tracts.

To demonstrate the clinical usefulness, two clinical measures, i.e., length and calcification density of calcified vessels, are computed. To observe the step-by-step performance of the proposed method, all intermediate results, along with manual delineation results, on one mammogram are provided in Fig. 10.

A. Parameter Setting

1) *Parameter Learning for Linear Structure Analysis*: Peak strength δ_s and peak distance δ_d are the two most important parameters in the parallel linear structure detector. Their best values are learned from the training samples. Specifically, we arbitrarily select 800 positive samples from a pool of the true parallel linear patterns collected from expert's annotations in 20 mammograms. Meanwhile, 800 negative samples, which include background and single linear structure patterns, are also prepared for a balanced learning. We randomly divide this training data into four sets and perform four-fold cross-validation to obtain a good parameter setting. In each fold of cross-validation, 600 positive and 600 negative samples are taken as training data, and the remaining 400 samples are treated as testing data. The best learned parameter settings of δ_s and δ_d are 7 and 25 (pixels), respectively, which achieve average sensitivity of 93.0% for the testing data in four folds of cross-validation, along with average specificity of 85.1%. These learned parameters for peak strength δ_s and distance threshold δ_d are used for all experiments performed below.

Our linear structure analysis method is tested on all 63 digital mammograms. For the performance analysis, we compare the

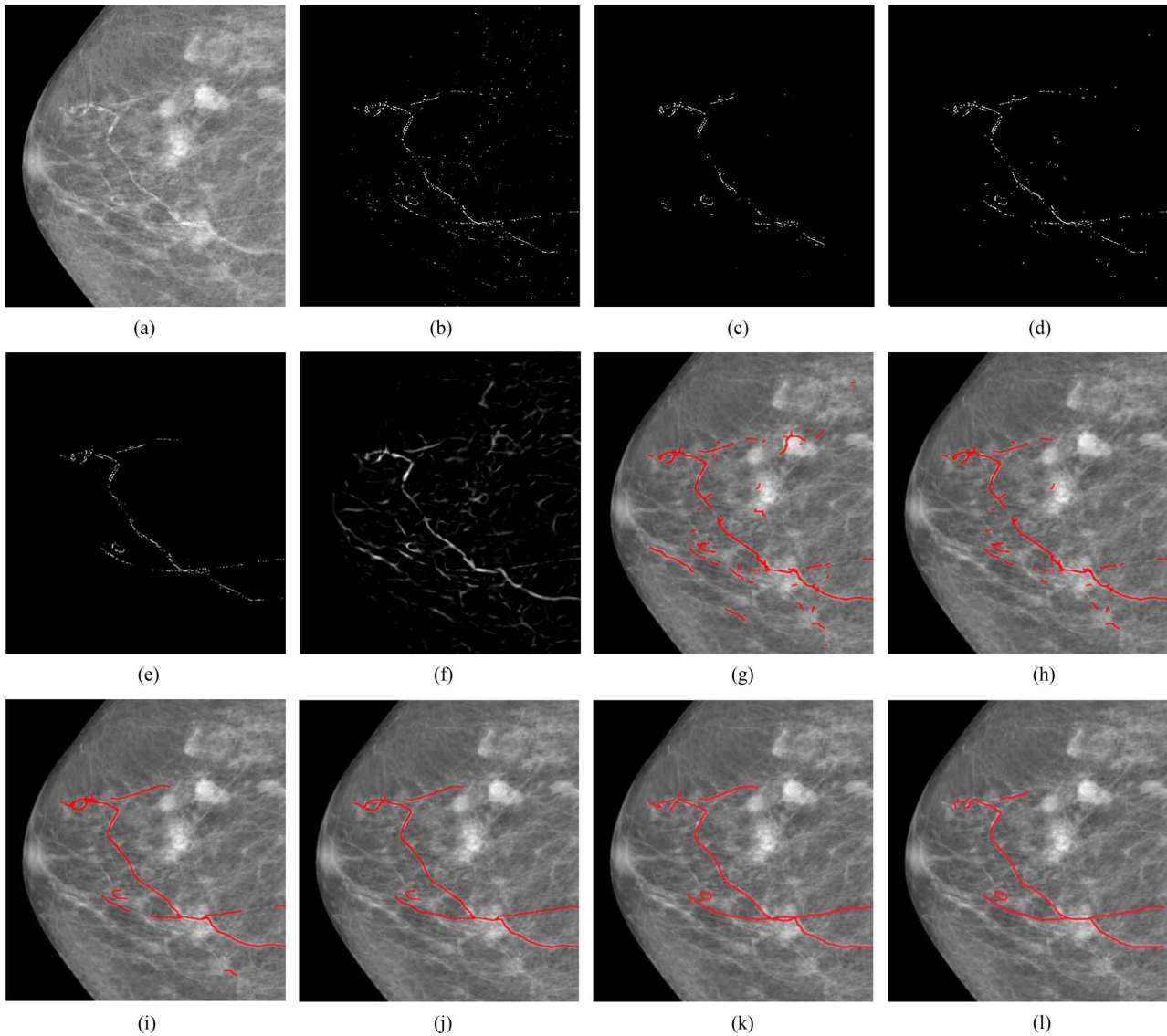


Fig. 10. Demonstration on a low-density case. (a) Original mammography. (b) Calcifications detected with the technique [1]. (c) Identified calcifications with parallel linear structures from (b). (d) Final result of linear structure analysis. (e) Calcifications selected by an expert. (f) Vesselness map. (g) Initial super-paths extracted by the tracking scheme with uncertainty. (h) Super-paths after eliminating ineligible super-paths. (i) Intermediate result of iteratively linking process. (j) Final result. (k), (l) Manual delineations by two experts.

computerized results with the expert's delineation results. As it is infeasible to manually pick the calcifications in a pixel-by-pixel fashion, we provide a user interface to allow user to draw a box to identify a group of true calcium deposition on the calcification map. Typical results can be found in Fig. 10(b)–(d), with the corresponding manual identifications from an expert shown in Fig. 10(e). From Fig. 10(d), we can see that the most desired calcium depositions are located and also the false calcification points are removed significantly. We asked the same two experts to prepare two sets of manual calcification selections. The overall detection performance of our method with respect to the first expert on the 63 mammograms reaches $92.6 \pm 2.2\%$ for sensitivity and $83.9 \pm 3.6\%$ for specificity. The sensitivity and specificity with respect to the second expert are $91.3 \pm 3.5\%$ and $82.7 \pm 4.1\%$, respectively.

2) *Settings of N_{samp} and z* : The number of sampling paths, N_{samp} , is set to 20 for each tracking seed in our study. Since the

uncertain vessel tracking process is driven by multiple calcification seeds, a higher setting of N_{samp} is not helpful in finding more true calcified vessels according to our experience. For the setting of the angle-against-distance ratio, z , in the iteratively linking process, it is set to 0.15 in the overall performance analysis. In our experience, a high value of ratio z will miss to establish some desirable linkages, whereas too small z will increase the establishment of false linkages.

B. Overall Performance Analysis

The overall performance of our proposed method is evaluated by comparing the computer-estimated results with two sets of manual delineations. There exist some disagreements between the two manual delineations, particularly in the cases with subtle BACs, or calcified vessels around dense tissues. Meanwhile, the inference of linkage ambiguity for the cases of vessels coming tortuously and deeply in and out of the mammographic views

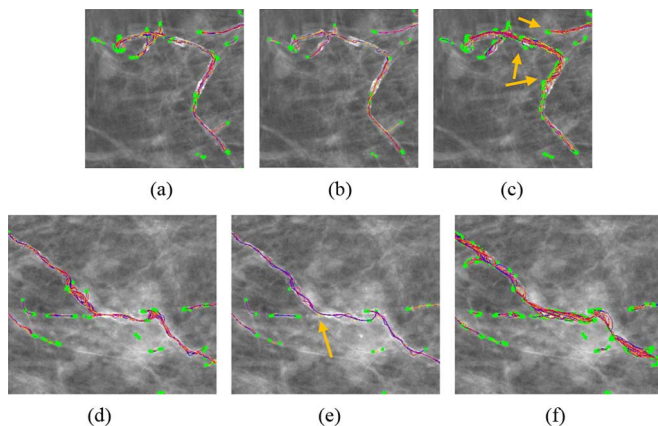


Fig. 11. Tracking results (with multiple seeds) by our method, Aylward's method, and particle filter. In each ROI, the green dots stand for terminations of computed tracts, and the tracts are drawn in various colors but not green. (a) and (d) show the results of tracking with uncertainty, and (b) and (e) show the results from Aylward's method. The vessel tracts delineated by particle filter are shown in (c) and (f).

may also lead to the disagreed delineations. Two baseline algorithms, Aylward's method [17] and particle filter [19], [20], are included here for comparison. In particular, the number of particles in the particle filter is set to 50 to produce the desirable results.

Fig. 11 compares two ROIs of tracking results with respect to our proposed method, Aylward's method, and particle filter. In general, vessel tracking with particle filter tends to generate more diffusive results, whereas Aylward's method may not provide sufficient tracts. Although our compiling and linking process may, to some extent, handle the diffusive and insufficient tracking results for these two methods, the undesirable linking results still cannot be avoided. For examples, too many termination points can easily enable the linking process to establish incorrect linkage [e.g., the linkages between the termination points as indicated by the yellow arrows in Fig. 11(c)]. Also, because of too many premature terminations from particle filter, the number of super-paths can be 2–3 folds more, compared to the number of super-paths from our tracking method, which also makes the linking problem more difficult and thus takes more time to finish the linking process. On the other hand, Aylward's method is not able to delineate the subtle ending point of the thinner tract [as indicated by the yellow arrow in Fig. 11(e)] and thus makes the linking process unable to generate a complete thinner tract.

In the following, the results of these two baseline methods and our method will be compared quantitatively to the two sets of manual delineation results, using three assessment metrics and two clinical measures as defined above. Also, the stability of our method will be tested by running our method for four times to compare the four sets of obtained results.

1) *Evaluation With Three Assessment Metrics*: Three assessment metrics, i.e., Diff_Ln, Miss_Ln, and FD_Ln, are used to compare the computer-generated results with the two sets of manual delineation results. Table I reports the mean \pm standard deviation for the three assessment metrics. The inter-observer differences (MD1-MD2) are also shown in Table I. The four sets of our results (by running our method for four times) are

TABLE I
COMPARISON OF THE COMPUTER-ESTIMATED RESULTS AND MANUAL DELINEATIONS USING THREE ASSESSMENT METRICS

	Diff_Ln	Miss_Ln	FD_Ln
CD1-MD1	4.27 \pm 5.55	3.75 \pm 5.90	1.61 \pm 3.59
CD2-MD1	3.90 \pm 4.43	3.21 \pm 4.74	1.63 \pm 4.45
CD3-MD1	4.15 \pm 4.88	3.21 \pm 5.40	1.78 \pm 4.04
CD4-MD1	3.76 \pm 3.72	3.02 \pm 4.21	1.64 \pm 4.09
Single-MD1	10.50 \pm 11.39	8.99 \pm 11.44	1.20 \pm 2.51
Particle-MD1	5.42 \pm 5.39	3.29 \pm 7.19	4.39 \pm 7.07
MD1-MD2	4.82\pm4.84	3.39\pm4.87	4.00\pm6.68
CD1-MD2	5.26 \pm 5.55	3.94 \pm 5.28	2.33 \pm 3.76
CD2-MD2	5.02 \pm 5.30	3.39 \pm 4.47	2.33 \pm 4.15
CD3-MD2	5.14 \pm 5.58	3.22 \pm 4.58	2.42 \pm 4.49
CD4-MD2	4.68 \pm 4.89	3.34 \pm 4.45	2.47 \pm 4.34
Single-MD2	9.85 \pm 10.44	8.97 \pm 10.59	1.88 \pm 3.74
Particle-MD2	6.02 \pm 7.35	3.18 \pm 3.98	4.92 \pm 5.92

denoted as "CD1," "CD2," "CD3," and "CD4," respectively. Detection results of Aylward's method are denoted as "Single" (as it is a single solution method), and results of particle filter are denoted as "Particle." In summary, we can see that the four sets of our results are quite close to each other, and vary less than inter-observer variation (shown in the row of "MD1-MD2" in Table I). Although fewer false vessels are detected by Aylward's method, significant amount of true calcified vessels are missed. The particle filter method achieves smaller missing rate than the proposed method, but it introduces more false-detected vessel segments.

2) *Evaluation With Two Clinical Measures*: To evaluate the clinical usefulness, two clinical measures, i.e., total lengths and calcium densities of calcified vessels, are computed from computer-estimated results and manual delineations for comparison. The calcification density of a vessel tract with calcium deposition is calculated as $\mathcal{A}_c/\mathcal{A}_v$, where \mathcal{A}_c is the mammographic imaged calcification area within the vessel and \mathcal{A}_v is the vessel area. For the computer-estimated results, we use the primitive detection result of the technique [1] to obtain \mathcal{A}_c , since results of our linear structure analysis may discard some true calcifications. The area of a vessel tract, \mathcal{A}_v , is computed as the area within the vessel tube which is dilated bilaterally in diameter from the identified vessel tract. The diameter of a vessel tract is estimated from the vesselness map as shown in our previous study [42]. The computation of \mathcal{A}_c for manual measurement is also based on the same calcification map as used in the computer-estimated measures. For manual definition of \mathcal{A}_v , the diameter information is also defined from the two experts. We compare the length and calcification density measurements with respect to the four sets of our results (by running our methods for four times), Aylward's method (single), particle filter, and two sets of manual delineation results. The mean \pm standard deviation statistics of total length for 'CD1' \sim 'CD4', "Single," "Particle," and 'MD1' \sim 'MD2' are 74.39 \pm 51.14 mm, 75.31 \pm 52.03 mm, 75.58 \pm 51.95 mm, 75.48 \pm 52.27 mm, **67.72 \pm 46.70 mm**, **80.71 \pm 51.14 mm**,

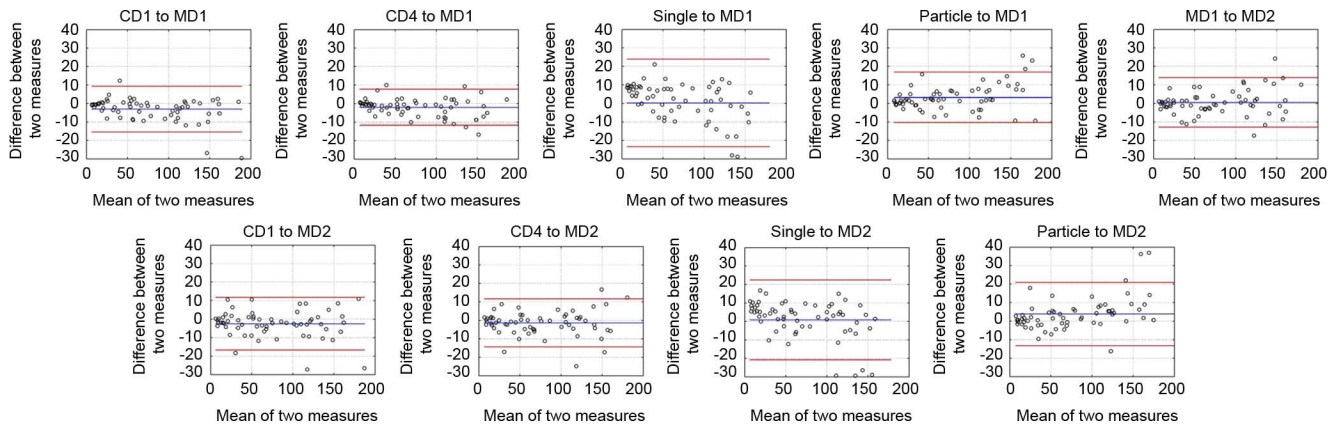


Fig. 12. Bland and Altman plots of total length measurement for the comparison between computer-estimated results and manual delineation results, and the two manual delineation results.

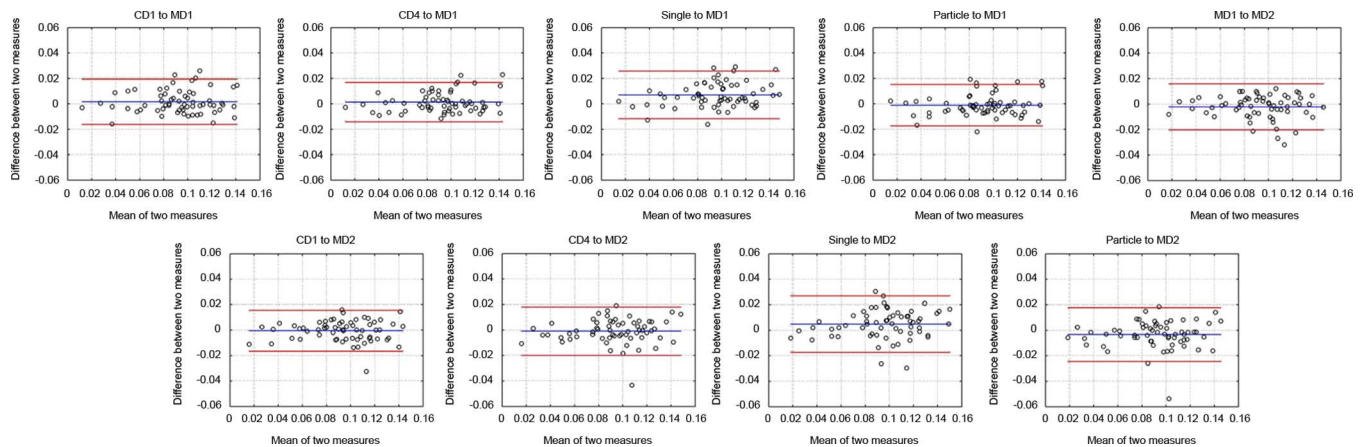


Fig. 13. Bland and Altman plots of calcification density measurement for the comparison between computer-estimated results and manual delineation results, and the two manual delineation results.

76.88 ± 52.07 mm, and 77.45 ± 53.54 mm, respectively. The mean \pm standard deviation statistics of calcification density for ‘CD1’ \sim ‘CD4’, “Single,” “Particle,” and ‘MD1’ \sim ‘MD2’ are $9.0\% \pm 2.89\%$, $9.23\% \pm 2.98\%$, $9.29\% \pm 2.95\%$, $9.27\% \pm 2.98\%$, $9.84\% \pm 3.07\%$, $9.02\% \pm 2.95\%$, $9.36\% \pm 2.91\%$, and $9.14\% \pm 2.83\%$, respectively.

Bland and Altman test [43] is further adopted to visualize the agreement of the two clinical measures between computer-estimated results and manual delineation results, as shown in Figs. 12 and 13 for the measurements of total length and calcification density, respectively. For saving space, Figs. 12 and 13 report only the plots of “CD1” and “CD4.” In a Bland and Altman plot, the horizontal and vertical axes stand for the mean and difference of two comparing measures, respectively. The blue line in a Bland and Altman plot is the mean difference of the two measures while the two red lines delimit the 95% confidence interval (CI) of the measure differences. In a Bland and Altman test of two clinical measurement sets, says “A” to “B,” if the measurement set “A” is in average larger than the set “B,” the mean difference (blue line) will be higher than 0. On the contrary, a negative mean difference suggests the measurement set “A” is in average less than the set “B.” A narrow range of the 95% CI of the measure differences, i.e., close distance between the two red lines, suggests that there is no significant difference

between the two measurement sets. In Fig. 12, it can be seen that the total length measurements of our two sets of results are close to the two sets of manual delineations. The length measurements from particle filters may also approach to the manual measurements, but hold wider range of 95% CIs and are also higher than manual measurements in average. Length measurements for Aylward’s method are lower than manual measurements, and their difference are quite significant. As it can be observed in Fig. 13, calcification density measurements from our results are quite close to MD1 and MD2, whereas density measurements of particle filter may be closer to MD1 than MD2. In average, density measurements with Aylward’s method are higher than all manual density measurements.

3) *Stability Analysis:* To illustrate the deviation between the four sets of our results, we plot the range spanned by mean \pm standard deviation of the four sets with the histograms of total length and calcification density measurements in Fig. 14, for all 63 mammograms. The mean \pm standard deviation statistics of the standard deviation of total length measurements over all 63 mammograms is 1.94 ± 2.01 mm, while the statistics of the standard deviation of calcification density measures is $0.36 \pm 0.23\%$. The mean measurements of the four sets of our results for the total length and calcification density are 75.19 ± 51.80 mm and $9.27\% \pm 2.93\%$, respectively. Comparing to these mean mea-

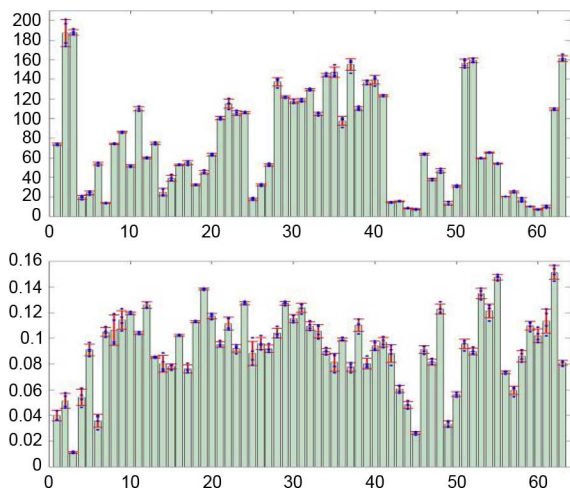


Fig. 14. Demonstration for the ranges of the mean \pm standard deviation of the four sets of our results on 63 mammograms (shown in horizontal axis). The top subfigure is for the total length measurements, and the bottom subfigure is for the calcification density measurements. In the two subfigures, the measurement range from “mean - standard” to “mean + standard deviation” in each mammogram is delimited with a red error bar. A blue dot represents a measurement result of our method.

surements, the variation among the four sets of our results are reasonably small. Thus our method is stable.

IV. DISCUSSION AND CONCLUSION

The hypothesis of relating the breast arterial calcification to women’s cardiovascular diseases has not been well studied [2]–[12]. For more insightful clinical investigation of this hypothesis, this paper introduces a pioneering computerized method to assist the delineation of calcified vessels in mammography and also the quantization of breast arterial calcification degree. To deal with the respective difficulties, we resort to Monte Carlo method to generate multiple sampling paths with a new vessel tracking with uncertainty scheme. Also, a compiling and linking process is further developed to organize the sampling paths and complete the disconnected calcified vessels.

The proposed algorithm is evaluated on 63 digital mammograms. Four sets of computer-generated results by the proposed method are compared with the two sets of manual delineations from two experts, by using three assessment metrics. Two baseline algorithms, Aylward’s method [17] and particle filter [19], [20], are also implemented for comparison. The final linked results of these two baseline algorithms are similarly evaluated with the three assessment metrics. According to Table I, the results of our proposed algorithm and the particle filter based method are close to the manual delineations. However, the particle filter results may detect more false vessel segments and hence may have larger difference to MD1 and MD2 in the metrics of Diff_Ln and FD_Ln as confirmed by our experimental results. The Aylward’s method detects less false segments, but fails to identify many true segments.

To test the clinical usefulness of our proposed method, the total length and calcification density measures are also computed from the four sets of our results, the results of Aylward’s method and particle filter, and manual delineations. Bland and

Altman test [43] is adopted to investigate degree of agreement between the computer-estimated and manual measures. Similar to the conclusion for three assessment metrics, the two clinical measurements from our algorithm and particle filter are closer to the measurements from MD1 and MD2. The particle filter results may have higher variation to the manual delineation results. Meanwhile, the total length measurements from particle filter may tend to have larger variation to the manual measurements, especially for the cases with longer calcified vessels; see Fig. 12. These results suggest that our proposed method can produce comparable results as manual delineations, but better than the two baseline algorithms.

According to Fig. 11, our tracking with uncertainty scheme may attain satisfactory results by comparing to the Aylward’s method and particle filter. Particle filter may generate more diffusive tracking results as it considers the appearance cue [19], [20]. Although Gaussian mixture is adopted to consider the calcification distribution, the appearance cue may fall short to regularize the tracking process effectively and thus introduces many premature terminations. As argued in the Section I, the appearance of a calcified vessel may be too complex to be helpful in our problem. Our tracking with uncertainty scheme instead looks for the next multiple tracking candidates with high vesselness values. In this case, our random tracking results can be more certain with help of vesselness cue. Although Aylward’s method may also utilize similar vesselness cue (Hessian analysis), only local maximum and single solution are considered. We can see that such local maximum strategy may miss some subtle but true vessel segments, as shown in Fig. 11(e). On the other hand, the local maximum constraint is relaxed in our tracking with uncertainty scheme by also considering other candidates with high vesselness values. Therefore, our tracking with uncertainty scheme can be considered as a method in-between Aylward’s method and particle filter. It holds both advantages of vesselness regularization with simple computation and also the multiple solutions with Monte Carlo method.

The major limitation of the proposed method is the lack of the consideration of breast density. Different parameter settings may be required to various degrees of breast density in mammography. In the future study, we will continue collecting more data and develop an algorithm to automatically compute the breast density on each subject. With sufficient dataset, we may be able to categorize breast density effectively with machine learning techniques. Then, we may be able to set adaptive parameters for different breast densities, for more accurate detection of calcified vessels in mammography.

In conclusion, the calcified vessels in mammography can be effectively detected by leveraging two underlying calcification and vesselness cues, along with uncertain vessel tracking and graphical linking techniques. Experiment results indicate that our proposed method can potentially replace the trivial and tedious manual delineations for providing the objective identification of BAC in mammography.

REFERENCES

- [1] H. P. Chan, K. Doi, S. Galhotra, C. J. Vyborny, H. Macmahon, and P. M. Jokich, “Image feature analysis and computer-aided diagnosis in digital radiography. 1. Automated detection of microcalcifications in mammography,” *Med. Phys.*, vol. 14, pp. 538–548, Jul./Aug. 1987.

- [2] A. H. E. M. Maas, Y. T. van der Schouw, W. P. T. M. Mali, and Y. van der Graaf, "Prevalence and determinants of breast arterial calcium in women at high risk of cardiovascular disease," *Am. J. Cardiol.*, vol. 94, pp. 655–659, Sep. 2004.
- [3] J. M. Kemmeren, P. A. H. van Noord, D. Beijerinck, J. Fracheboud, J. D. Banga, and Y. van der Graaf, "Arterial calcification found on breast cancer screening mammograms and cardiovascular mortality in women—The DOM project," *Am. J. Epidemiol.*, vol. 147, pp. 333–341, Feb. 1998.
- [4] M. A. Rotter, P. F. Schnatz, A. A. Currier, and D. M. O'Sullivan, "Breast arterial calcifications (BACs) found on screening mammography and their association with cardiovascular disease," *Menopause*, vol. 15, pp. 276–281, Mar./Apr. 2008.
- [5] M. Kataoka, R. Warren, R. Luben, J. Camus, E. Denton, E. Sala, N. Day, and K.-T. Khaw, "How predictive is breast arterial calcification of cardiovascular disease and risk factors when found at screening mammography?," *Am. J. Roentgenol.*, vol. 187, pp. 73–80, 2006.
- [6] P. Crystal, E. Crystal, J. Leor, M. Friger, G. Katzinovitch, and S. Strano, "Breast artery calcium on routine mammography as a potential marker for increased risk of cardiovascular disease," *Am. J. Cardiol.*, vol. 86, pp. 216–217, Jul. 2000.
- [7] J. M. Kemmeren, D. Beijerinck, P. A. H. van Noord, J. D. Banga, J. J. M. Deurenberg, F. A. Pameijer, and Y. vanderGraaf, "Breast arterial calcifications: Association with diabetes mellitus and cardiovascular mortality—Work in progress," *Radiology*, vol. 201, pp. 75–78, Oct. 1996.
- [8] P. F. Schnatz, K. A. Marakovits, and D. M. O'Sullivan, "The association of breast arterial calcification and coronary heart disease," *Obstetr. Gynecol.*, vol. 117, pp. 233–241, 2011.
- [9] M. H. Zgheib, S. S. Buchbinder, N. Abi Rafeh, M. Elya, C. Raia, K. Ahern, M. C. Smith, T. Costantino, M. J. Flory, J. C. Lafferty, and M. R. Castellanos, "Breast arterial calcifications on mammograms do not predict coronary heart disease at coronary Angiography¹," *Radiology*, vol. 254, pp. 367–373, Feb. 2010.
- [10] J. Reddy, J. P. Bilezikian, S. J. Smith, and L. Mosca, "Reduced bone mineral density is associated with breast arterial calcification," *J. Clin. Endocrinol. Metabol.*, vol. 93, pp. 208–211, Jan. 2008.
- [11] V. Duhn, E. T. D'Orsi, S. Johnson, C. J. D'Orsi, A. L. Adams, and W. C. O'Neill, "Breast arterial calcification: A marker of medial vascular calcification in chronic kidney disease," *Clin. J. Am. Soc. Nephrol.*, vol. 6, pp. 377–382, Feb. 2011.
- [12] M. Cetin, R. Cetin, N. Tamer, and S. Kelekci, "Breast arterial calcifications associated with diabetes and hypertension," *J. Diabetes Complicat.*, vol. 18, pp. 363–366, Nov./Dec. 2004.
- [13] H. Wada, F. Hirano, T. Kuroda, and M. Shiraki, "Breast arterial calcification and hypertension associated with vertebral fracture," *Geriatr. Gerontol. Int.*, vol. 12, pp. 330–335, 2012.
- [14] H. Wada, M. Kitada, K. Sato, T. Sasajima, N. Miyokawa, and T. Kuroda, "Prevalence of breast arterial calcification by mammography contributes to breast cancer," *Breast Cancer*, pp. 1–4, 2011.
- [15] M. Schaap, R. Manniesing, I. Smal, T. van Walsum, A. van der Lugt, and W. Niessen, "Bayesian tracking of tubular structures and its application to carotid arteries in CTA," in *Proc. Med. Image Computing Computer-Assisted Intervent.*, 2007, pp. 562–570.
- [16] W. C. K. Wong and A. C. S. Chung, "Probabilistic vessel axis tracing and its application to vessel segmentation with stream surfaces and minimum cost paths," *Med. Image Anal.*, vol. 11, pp. 567–587, Dec. 2007.
- [17] S. R. Aylward and E. Bullitt, "Initialization, noise, singularities, and scale in height ridge traversal for tubular object centerline extraction," *IEEE Trans. Med. Imag.*, vol. 21, no. 2, pp. 61–75, Feb. 2002.
- [18] M. Descoteaux, D. L. Collins, and K. Siddiqi, "A geometric flow for segmenting vasculature in proton-density weighted MRI," *Med. Image Anal.*, vol. 12, pp. 497–513, Aug. 2008.
- [19] C. Florin, N. Paragios, and J. Williams, "Globally optimal active contours, sequential Monte Carlo and on-line learning for vessel segmentation," *Proc. Comput. Vis., EVC 2006*, pt. 3, pp. 476–489, 2006.
- [20] C. Florin, N. Paragios, and J. Williams, "Particle filters, a quasi-Monte-Carlo-solution for segmentation of coronaries," *Proc. Med. Image Comput. Computer-Assisted Intervent., MICCAI*, pt. 1, pp. 246–253, 2005.
- [21] O. Friman, M. Hindennach, C. Kühnel, and H.-O. Peitgen, "Multiple hypothesis template tracking of small 3-D vessel structures," *Med. Image Anal.*, vol. 14, pp. 160–171, 2010.
- [22] J. Staal, M. D. Abramoff, M. Niemeijer, M. A. Viergever, and B. van Ginneken, "Ridge-based vessel segmentation in color images of the retina," *IEEE Trans. Med. Imag.*, vol. 23, no. 4, pp. 501–509, Apr. 2004.
- [23] P. Zou, P. Chan, and P. Rockett, "A model-based consecutive scan-line tracking method for extracting vascular networks from 2-D digital subtraction angiograms," *IEEE Trans. Med. Imag.*, vol. 28, no. 2, pp. 241–249, Feb. 2009.
- [24] M. Schaap, I. Smal, C. Metz, T. van Walsum, and W. Niessen, "Bayesian tracking of elongated structures in 3-D images," in *Information Processing Medical Imaging—IPMI 2007*, Kerkraade, The Netherlands, 2007, pp. 74–85.
- [25] R. Manniesing, M. A. Viergever, and W. J. Niessen, "Vessel axis tracking using topology constrained surface evolution," *IEEE Trans. Med. Imag.*, vol. 26, no. 3, pp. 309–316, Mar. 2007.
- [26] X. Huang and D. N. Metaxas, "Metamorphs: Deformable shape and appearance models," *IEEE Trans. Pattern Anal. Mach. Intell.*, vol. 30, no. 8, pp. 1444–1459, Aug. 2008.
- [27] D. Lesage, E. D. Angelini, I. Bloch, and G. Funka-Lea, "A review of 3-D vessel lumen segmentation techniques: Models, features and extraction schemes," *Med. Image Anal.*, vol. 13, pp. 819–845, 2009.
- [28] S. Zhang, Y. Zhan, M. Dewan, J. Huang, D. N. Metaxas, and X. S. Zhou, "Towards robust and effective shape modeling: Sparse shape composition," *Med. Image Anal.*, vol. 16, pp. 265–277, 2012.
- [29] J. Ge, H. P. Chan, B. Sahiner, C. Zhou, M. A. Helvie, J. Wei, L. M. Hadjiiski, Y. Zhang, Y. T. Wu, and J. Shi, "Automated detection of breast vascular calcification on full-field digital mammograms," in *Proc. SPIE Med. Imag.*, San Diego, CA, 2008, pp. 691517.1–691517.7.
- [30] J. Ge, B. Sahiner, L. M. Hadjiiski, H. P. Chan, J. Wei, M. A. Helvie, and C. Zhou, "Computer aided detection of clusters of microcalcifications on full field digital mammograms," *Med. Phys.*, vol. 33, pp. 2975–2988, Aug. 2006.
- [31] H. P. Chan, S. C. Lo, B. Sahiner, K. L. Lam, and M. A. Helvie, "Computer-aided detection of mammographic microcalcifications: Pattern recognition with an artificial neural network," *Med. Phys.*, vol. 22, pp. 1555–67, Oct. 1995.
- [32] A. Frangi, W. Niessen, K. Vincken, and M. Viergever, "Multiscale vessel enhancement filtering," *Med. Image Comput. Computer-Assisted Intervent.*, pp. 130–137, 1998.
- [33] M. Lazar and A. L. Alexander, "Bootstrap white matter tractography (BOOT-TRAC)," *Neuroimage*, vol. 24, pp. 524–32, Jan. 2005.
- [34] D. K. Jones, "Tractography gone wild: Probabilistic fibre tracking using the wild bootstrap with diffusion tensor MRI," *IEEE Trans. Med. Imag.*, vol. 27, no. 9, pp. 1268–1274, Sep. 2008.
- [35] P. Hagmann, J. P. Thiran, L. Jonasson, P. Vandergheynst, S. Clarke, P. Maeder, and R. Meuli, "DTI mapping of human brain connectivity: Statistical fibre tracking and virtual dissection," *NeuroImage*, vol. 19, pp. 545–554, 2003.
- [36] Y. Shi, Z. Tu, A. L. Reiss, R. A. Dutton, A. D. Lee, A. M. Galaburda, I. Dinov, P. M. Thompson, and A. W. Toga, "Joint sulcal detection on cortical surfaces with graphical models and boosted priors," *IEEE Trans. Med. Imag.*, vol. 28, no. 3, pp. 361–373, Mar. 2009.
- [37] O. Friman, A. Hennemuth, A. Harloff, J. Bock, M. Markl, and H.-O. Peitgen, "Probabilistic 4D blood flow tracking and uncertainty estimation," *Med. Image Anal.*, vol. 15, pp. 720–728, 2011.
- [38] O. Friman, A. Hennemuth, A. Harloff, J. Bock, M. Markl, and H.-O. Peitgen, "Probabilistic 4D blood flow mapping," in *Med. Image Comput. Computer-Assisted Intervent.*, Beijing, China, 2010, pp. 416–423.
- [39] L. Vincent and P. Soille, "Watersheds in digital spaces—An efficient algorithm based on immersion simulations," *IEEE Trans. Pattern Anal. Mach. Intell.*, vol. 13, no. 6, pp. 583–598, Jun. 1991.
- [40] N. Otsu, "A thresholding selection method from gray-level histogram," *IEEE Trans. Syst., Man Cybern.*, vol. 9, pp. 62–66, 1979.
- [41] X. Ren, C. C. Fowlkes, and J. Malik, "Learning probabilistic models for contour completion in natural images," *Int. J. Comput. Vis.*, vol. 77, pp. 47–63, May 2008.
- [42] J. Z. Cheng, E. B. Cole, E. D. Pisano, and D. Shen, "Detection of arterial calcification in mammograms by random walks," in *Inf. Process. Med. Imag.*, Williamsburgh, VA, 2009, pp. 713–724.
- [43] J. M. Bland and D. G. Altman, "Comparing methods of measurement: Why plotting difference against standard method is misleading," *Lancet*, vol. 346, pp. 1085–1087, 1995.